C.L. Bottasso, P. Pizzinelli, C.E.D. Riboldi, L. Tasca
*LiDAR-Enabled Model Predictive Control of Wind Turbines with Real-Time Capabilities*
Renewable Energy, Vol. 71, 2014, p. 442-452
doi:10.1016/j.renene.2014.05.041

# LiDAR-enabled model predictive control of wind turbines with real-time capabilities

C.L. Bottasso[a,b,*], P. Pizzinelli[c], C.E.D. Riboldi[b], L. Tasca[b]

[a] *Wind Energy Institute, Technische Universität München, Boltzmannstraße 15, D-85748 Garching bei München, Germany*
[b] *Dipartimento di Scienze e Tecnologie Aerospaziali, Politecnico di Milano, Via La Masa 34, I-20156 Milano, Italy*
[c] *Dipartimento di Elettronica, Informazione e Bioingegneria, Politecnico di Milano, Via Ponzio 34/5, I-20133 Milano, Italy*

**Abstract**

We consider LiDAR-enabled model-based collective pitch and torque controllers that can be implemented onboard a wind turbine in a hard real-time environment, in the sense that they can be computed efficiently on standard computer hardware and that require a fixed deterministic number of operations at each call.

At first, we show that linear parameter varying wind-scheduled models provide for a reasonable approximation (for control purposes) of the wind turbine response over its entire operating regime. Based on these results, we formulate two model predictive controllers making use of such wind-scheduled linear models and a quadratic cost. The first controller is based on a classical constrained receding horizon approach that leads to the efficient on-line solution of a quadratic problem. The second can be interpreted as its steady-state unconstrained approximation; its implementation is straightforward and leads to the off-line computation of gain matrices that are then wind-scheduled at run time.

Both controllers are tested in a high fidelity environment comprising of both a LiDAR and an aeroservoelastic simulator, in deterministic and unfrozen turbulent wind conditions. The numerical experiments show that the receding horizon controller outperforms a standard non-LiDAR-enabled one, as expected and as already reported by other authors. More interestingly, the second simpler controller is shown to provide for an almost similar performance of the more sophisticated one, although at a much lower and trivial computational cost. This behavior is interpreted as being due to the fact that, given the high disturbance level and the frequent solution update, even a rough approximation of the control problem is still capable of capturing the essence of the LiDAR preview information.

*Keywords:*
Wind turbine control, LiDAR, Predictive control, Receding horizon, Non-homogeneous LQR, Unfrozen turbulence

*Corresponding author, *Tel.:* +49-89-289-16680; *Fax:* +49-89-289-16611.
*Email address:* carlo.bottasso@tum.de (C.L. Bottasso)

**Notation**

| | |
|---|---|
| $A$ | Rotor area |
| $C_Q$ | Aerodynamic torque coefficient |
| $C_T$ | Aerodynamic thrust coefficient |
| $J$ | Cost function |
| $J_g$ | Generator inertia |
| $J_r$ | Rotor inertia |
| $Q_e$ | Electrical torque |
| $Q_l$ | Mechanical torque loss |
| $Q_{e_c}$ | Commanded electrical torque |
| $R$ | Rotor radius |
| $S_u$ | Spectrum amplitude of unfrozen turbulence |
| $T_c$ | Wind estimate update time |
| $T_e$ | Characteristic time of electrical generator |
| $T_f$ | Prediction window length |
| $U_j$ | LiDAR measured wind speed at point $j$ |
| $V$ | Rotor-effective wind speed |
| $V_m$ | Moving average of rotor-effective wind speed |
| $c_t$ | Reduced tower damping |
| $d$ | Tower top fore-aft displacement |
| $d_i$ | $i$-th focal distance |
| $f_i$ | $i$-th frequency of turbulent wind field |
| $k_t$ | Reduced tower stiffness |
| $m_t$ | Reduced tower mass |
| $t$ | Time |
| $u$ | Longitudinal wind speed component |
| $\boldsymbol{A}$ | State matrix |
| $\boldsymbol{B}$ | Control matrix |
| $\boldsymbol{G}$ | Disturbance matrix |
| $\boldsymbol{P}$ | Solution of the algebraic Riccati equation |
| $\boldsymbol{Q}$ | State weight matrix |
| $\boldsymbol{Q}_f$ | Final state weight matrix |
| $\boldsymbol{R}$ | Control input weight matrix |
| $\boldsymbol{u}$ | Control input vector |

| | |
|---|---|
| $\boldsymbol{w}$ | Vector of wind disturbances |
| $\boldsymbol{x}$ | State vector |
| $\Omega$ | Rotor speed |
| $\beta$ | Blade collective pitch |
| $\beta_c$ | Commanded blade collective pitch |
| $\nu$ | Integral of rotor speed |
| $\omega$ | Characteristic pulsation |
| $\phi_i$ | $i$-th phase of turbulent wind field |
| $\rho$ | Air density |
| $\tau$ | Dummy time variable |
| $\xi$ | Damping ratio |
| $N_d$ | Number of focal distances |
| $N_f$ | Number of frequencies |
| $N_s$ | Number of stops over scan pattern |
| $N_w$ | Number of points for Lorentz weighting discretization |
| $\dot{(\cdot)}$ | Derivative wrt time, $\mathrm{d}\cdot/\mathrm{d}t$ |
| $\ddot{(\cdot)}$ | Second derivative wrt time, $\mathrm{d}^2\cdot/\mathrm{d}t^2$ |
| $(\cdot)^*$ | Reference value |
| $(\cdot)^T$ | Transpose |
| $\Delta(\cdot)$ | Perturbation, small increment |
| BEM | Blade element momentum |
| DEL | Damage equivalent load |
| EOG | Extreme operative gust |
| LiDAR | Light detection and ranging |
| LQR | Linear quadratic regulator |
| NHLQR | Non-homogeneous linear quadratic regulator |
| RHC | Receding horizon control |

## 1. Introduction

Modern wind turbines are equipped with controllers that, using both blade pitch and electrical torque, regulate the machine over its entire operating envelope, while reacting to gusts and wind turbulence. The majority of these controllers operate on the basis of the classical feedback principle: at each given time instant, control inputs are calculated from measured outputs available at that same time and possibly in

the near past. In this work we consider control techniques based on preview information, available from the current instant up to one in the near future, enabled by measurements of the incoming flow field in front of the rotor provided by a LiDAR (Light Detection And Ranging) sensor.

LiDARs, which can be mounted onboard the machine for instance in the nacelle or the spinner, illuminate by means of suitable light beams water and dust particles transported by the wind flow and, by interpreting their reflections, provide for a spatial description of the wind velocity field, typically at distances of the order of tens of meters ahead of the turbine, i.e. several seconds in the future [1, 2, 3]. By its very definition, classical feedback control is invariably late, since it reacts to wind changes that have already taken place and that are already affecting the response of the machine. On the other hand, the use of LiDAR-enabled preview information anticipates the effects of such wind changes, with possible beneficial improvements in terms of fatigue and maximum load alleviation, as well as overspeed reduction and power capture.

The translation of any such performance improvement in a reduction of the cost of energy has yet to be fully explored. The easiest to exploit improvement would probably be a resizing of some fatigue-driven components of the machine. A similar beneficial effect on extreme-load-driven components would be much less straightforward to achieve, as extreme design-driving loads are often taking place in emergency or storm conditions when closed-loop control is of little or no use. In those situations when extreme loads do indeed take place in closed-loop control conditions, in order to resize a component exploiting a LiDAR-induced load alleviation, one would have to assume the continuous availability of the LiDAR sensor, which on the other hand can be affected by environmental conditions such as rain, fog or snow. Notwithstanding these not yet fully understood problems, the possible benefits of LiDAR technology have spurred an active interest in the wind turbine control community [4, 5, 6, 7, 8, 9, 10, 11, 12, 13].

There are various control schemes that are capable of exploiting the preview information provided by knowledge of the incoming wind. Two of them are considered in this work. The first approach is a classical constrained predictive receding horizon controller (RHC), based on a parameter varying (wind-scheduled) linear model [14, 5]. The second is an extension of the linear quadratic regulator (LQR), accounting for an exogenous input (i.e. the wind); this second formulation can be interpreted as a steady-state unconstrained approximation of RHC for an infinite prediction horizon. This second control scheme will be referred to in the following as non-homogeneous LQR (NHLQR) [15].

These controllers share the same theoretical basis, as both are model-based optimal controllers seeking the minimization of a quadratic cost. Furthermore, they are considered here because they both have real-time capabilities, in the sense that they require a computational cost that is compatible, on current hardware, with the typical activation frequencies necessary to control a wind turbine, and both imply a fixed deterministic number of operations per activation. RHC allows one to consider linear inequality constraints and makes a more sophisticated use of the preview information; although it is real-time capable when implemented with

ad hoc solvers as done here [16], it is computationally demanding. On the other hand, NHLQR has a trivial computational cost, since its gain matrices can be pre-computed off-line and then wind-scheduled at run time, but it does not allow for constraints and treats the wind information in a more approximate way.

A first goal of this paper is to show that a wind-scheduled linear model can provide for a reasonable (for control purposes) approximation of the wind turbine response. This justifies its use in the design of model-based controllers, and it is the key for the satisfaction of the real-time requirement. In fact, if a non-linear model were needed, as advocated for example in Refs. [8, 17], the implementation of a predictive controller would not only be more expensive, but would most probably require a variable number of iterations. Unless further approximations were to be introduced in the solution process, this would necessarily lead to a non-deterministic number of operations per activation, which would further hinder a hard real-time implementation of the controller.

A second goal of this paper is to show that even a quite rough approximation of the control problem, as the one provided by the NHLQR formulation considered here, can still provide for a good performance. This is due to the fact that, as it is often the case in the solution of optimization problems in the presence of disturbances (see e.g. Ref. [27]), it is probably not necessary to provide for an accurate solution of the predictive control problem. In fact, the current problem is affected by considerable disturbances, including wind turbulence, distortion and mixing of the flow in its travel towards the rotor plane, noise in the LiDAR and all other sensors, time delays and model mismatch. Additionally, in model predictive control only the computed control inputs at the very next time instant are fed to the plant, while the rest of the solution is discarded and the optimization is immediately repeated on a forward shifted time horizon. In such a scenario of high disturbance and frequent updates, a detailed and high accuracy solution of the control problem over a long prediction window is probably not necessary, since what is more important is a correct capturing of the short-term effects of the preview information.

The paper starts by describing a LiDAR simulator, which is included in the overall virtual environment so as to increase its fidelity. In fact, the LiDAR sensor operates a strong filtering action on the wind measurement due to the volumetric and temporal averages that it performs, a low-pass effect that is particularly important in turbulent wind conditions [3, 4, 18, 6]. An unfrozen [21] wind model is implemented in the simulator, this way avoiding Taylor's frozen turbulence hypothesis [20] and accounting for the evolution of the turbulent wind field from the LiDAR measurement locations to the rotor disk. Next, the two predictive controllers are formulated and then tested in a high-fidelity simulation environment, using a comprehensive aeroservoelastic wind turbine model. This level of sophistication is considered necessary for the realism of the testing conditions, because it introduces a model mismatch between the plant and the reduced model used for control synthesis. Finally, the controllers are tested in deterministic gusts and both frozen and unfrozen turbulent wind conditions, and compared to a standard feedback controller.

The results support the hypothesis here put forward, in fact showing that the rather rough solution provided by NHLQR, although not as good as RHC, still outperforms the reference non-predictive controller. While for the implementation onboard a wind turbine one will certainly want to use the best performing controller available (RHC in this case), the indication that approximations are indeed possible can lead to future improvements and computational cost reductions.

## 2. Wind preview information

In order to feed the controllers considered in this work with realistic LiDAR measurements of the incoming wind, a LiDAR simulator was developed that accounts for the principal physical processes of the sensor [2].

A LiDAR emitter produces a straight beam characterized by very low dispersion, which is moved so as to describe a certain desired pattern (e.g., a circle). When a beam is emitted in a given direction, a number of measurements along its trajectory is collected at different focal distances from the source. The time required for a complete travel of the emitter along the prescribed pattern basically depends on three factors: the complexity of the pattern, the number of focal distances along the beam for every stop over the considered pattern, and, finally, the number of such stops. Depending on the choice of parameters, the collection of a full array of flow field samples over the whole pattern may take of the order of a few seconds. The maximum distance between the source and the measurement point furthest away from the turbine can be of the order of 1.5 rotor diameters even for large multi-MW turbines [2], which translates into a LiDAR prediction window of the order of some seconds into the future.

Measuring wind speed at a given point in space involves processing the echo coming from particles illuminated by the LiDAR beam focused at that point. The measured wind speed actually results from an average of the speed of multiple fluid particles crossing the beam in proximity of the focal point. In order to account for this process, the LiDAR-measured wind speed is computed in the simulation environment as a Lorentz weighted average of the true wind speed along the beam [1]. The weighting function is centered at each considered focal distance, and its characteristic span increases with the distance from the emitter; therefore, for small distances the resulting measure accounts primarily for particles in close proximity of the focal distance, while for larger ones it also includes particles quite away from the focus, resulting in a significant spatial average. Furthermore, on account of the cyclops effect [19], the wind speed component actually measured by the LiDAR sensor is only the one lying along the beam direction; this is obtained in the simulator simply by projecting the real wind speed vector along the beam direction.

A time-dependent prediction of the equivalent wind speed component normal to the rotor plane is obtained as follows. Considering the LiDAR configuration depicted in Fig. 1, $\theta_j$ is the angle between the LiDAR beam passing through the generic measurement point $j$ and the rotor axis, while $U_j$ is the LiDAR-measured wind speed component. The corresponding rotor orthogonal wind component is readily computed as $V_j =$

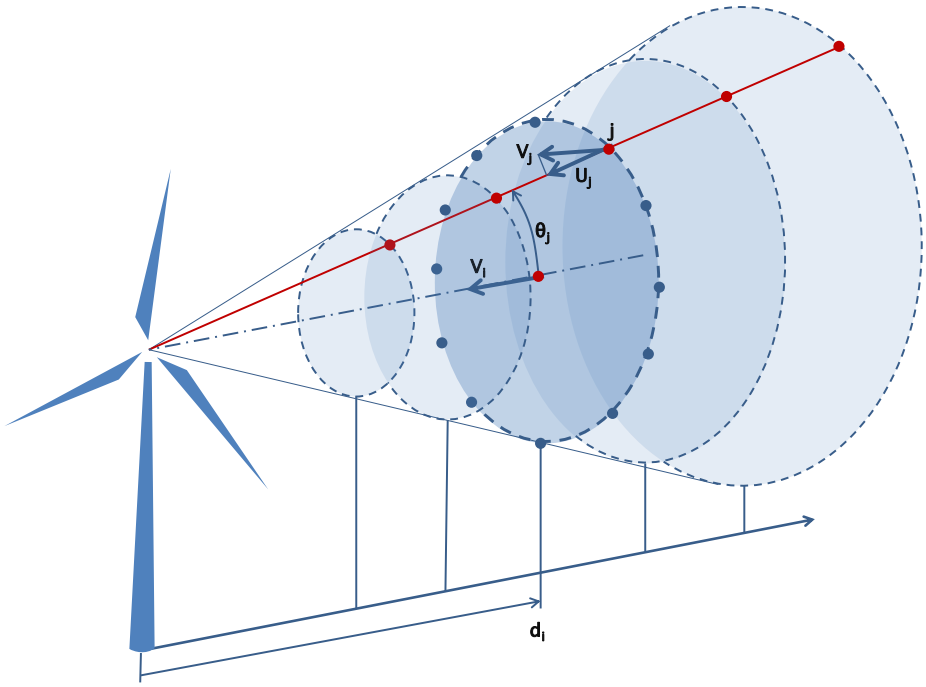


Figure 1: Schematic view of the LiDAR wind measurement process.

$U_j/\cos\theta_j$. The wind speed values $V_j$ at the various points over the scan pattern at the generic $i$-th focal distance are then averaged, resulting in a series of wind samples $V_i$, one for each focal distance ahead of the sensor, which are expressed as

$$V_i = \frac{1}{N_s}\sum_{j=1}^{N_s} V_j, \quad i = 1, \ldots, N_d, \tag{1}$$

where $N_s$ is the number of stops over the pattern and $N_d$ the number of focal distances. At every stop of the beam along the prescribed pattern, $N_d$ new measurements are simultaneously collected at all focal distances along the beam, allowing for a partial update of the pattern-averaged samples. The partial update is implemented in the following manner: for each focal distance $d_i$, a number of wind measurements equal to the number $N_s$ of prescribed stops along the pattern is stored in a buffer; every time a new measurement becomes available, it replaces the value stored in the buffer at the corresponding stop during the previous scan of the pattern. Next, the resulting array of pattern-averaged samples is converted into a time sequence by computing the time delay $\Delta t_i$ at each focal plane, i.e. the time taken by a fluid particle to travel the distance between that focal plane and the emitter. This is obtained by dividing all focal distances $d_i$ by the average wind speed $V_a$ in a direction orthogonal to the focal planes, i.e.

$$\Delta t_i = \frac{d_i}{V_a}. \tag{2}$$

Finally, the time histories at each focal plane are averaged among themselves, completing the averaging operation over the complete volume scanned by the LiDAR:

$$V(t) = \sum_{i=1}^{N_d} V_i(t + \Delta t_i). \tag{3}$$

The result is a single value of predicted wind for each time instant [18].

In the present analysis, the selected scan pattern has a circular shape, as shown in Fig. 1. More complex patterns, potentially capable of providing for a richer description of the wind spatial distribution, do not seem to provide substantial advantages in performance [22], at least when the information is used to drive a collective pitch controller. In the case considered here, the LiDAR hardware is fixed with respect to the nacelle and it does not spin with the rotor. The beam stops at $N_s = 12$ uniformly spaced stops over a circular trajectory, while $N_d = 5$ equally spaced focal distances have been used. The maximum focal distance is 1.5 diameters ahead of the hub; at this station, the circular pattern has the same diameter of the wind turbine rotor. As a consequence of this choice of parameters, five measurements are obtained every 30 deg of the LiDAR beam revolution over the pattern. For every stop along the circular trajectory and at every focal distance, the LiDAR simulator provides a speed value based on Lorentz weighting of $N_w = 100$ measurements along the beam, the weighting function being centered at that focal distance and having its corresponding characteristic span. It is assumed that covering the full pattern takes 2.4 sec of physical time. The wind estimate receives a partial update at every stop along the circular pattern, and the resulting update time of the wind information is consequently $T_c = 0.2$ sec.

By averaging along the light beam by Lorentz weighting and then over the samples of the scanning pattern and at multiple focal distances, a LiDAR performs an intrinsic low-pass filtering action of the wind field in space and time. Particularly in turbulent wind conditions, the ability of a LiDAR sensor of capturing only the lower part of the frequency spectrum of the flow field is very useful for control purposes. In fact, the slowly varying fluctuations and large eddies of the flow are precisely the ones whose effects can be compensated with a collective pitch and torque controller [3, 18]. On the other hand, the faster temporal turbulent scales and small eddies in the flow can not be directly affected, due to the limited actuation speed of the machine (finite temporal bandwidth) and to the full span pitch control that changes the angle of attack of the whole blade (finite spatial bandwidth).

To illustrate the filtering effect of the LiDAR sensor, a IEC category A turbulent wind field with an average speed of 15 m/sec is considered. Figure 2 shows the coherence [3] between the LiDAR measurement and the horizontal rotor effective wind speed. Coherence was estimated using Welch averaged periodogram method (see Refs. [23, 24]), by dividing the sampled time histories into a suitable number of Hamming-windowed and 25% overlapped sections of equal length, based on the sampling frequency and the number of available samples. This diagram confirms that there is a good agreement between LiDAR measurements and the real

wind at low frequencies, while the sensor operates a filtering action in the higher band of the spectrum.

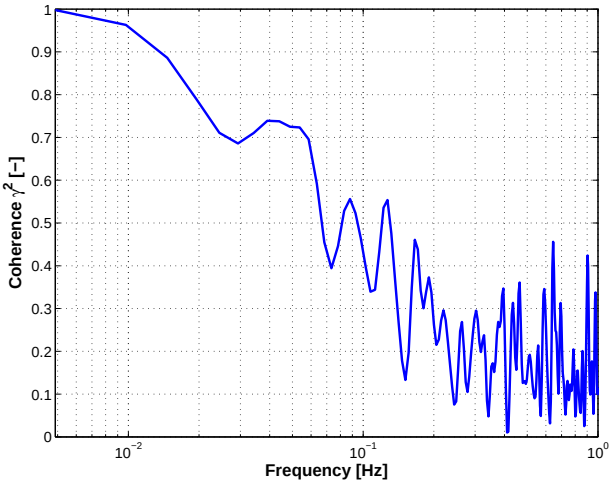


Figure 2: Coherence diagram for a 600 sec time history of IEC category A turbulent wind, between LiDAR measurements and rotor effective wind speed.

The formulation of Ref. [22] was used to avoid Taylor's frozen turbulence hypothesis [20, 21] in the LiDAR model implementation; this way, the temporal evolution of the flow in its travel from measurement points to the rotor disk is explicitly accounted for by a dynamic model of the free stream. Although such a model is important for removing the assumption of a frozen turbulent flow that is "rigidly" convected towards the wind turbine, its effect on the performance of predictive controllers similar to the ones discussed here has been shown to be not very relevant, and it can be assimilated to a further disturbance effect [22].

The theoretical model used in this work to generate an unfrozen turbulent field is that of Kristensen and Veers [25, 26], as adapted to wind power applications in Ref. [21]. A time history of the wind at a given position in space can be generated by summing to a reference constant value the contributions of a series of sinusoidal signals characterized by $N_f$ different frequencies:

$$\Delta u(t) = \sum_{i=1}^{N_f} S_u(f_i) \cos(2\pi f_i t + \phi_i), \tag{4}$$

where $\Delta u$ is a perturbation to the reference longitudinal wind component, $f_i$ is the frequency of the $i$-th sinusoid and $S_u(f_i)$ its amplitude. The random phase $\phi_i$ is correlated to the phases of other points in space, in such a way as to maintain the desired cross-wind coherence properties of turbulence [21]. An unfrozen wind time history can be obtained by suitably blending the characteristic phases $\phi_{i,1}$ and $\phi_{i,2}$ of two different turbulent wind time histories [21], obtained by using two distinct random seeds. Blending is carried out by

performing for every time instant a weighted average of the two histories as

$$\Delta u(t+\Delta t) = \sum_{i=1}^{N_f} S_u(f_i) \cos\left(2\pi f_i t + w_i \phi_{i,1} + (1-w_i)\phi_{i,2}\right), \tag{5}$$

where the semi-empirical weighting functions $w_i$ depend on the distance ahead of the rotor [25].

This formulation is used to account for the evolution of the turbulent flow field from the points where the LiDAR performs its measurements upstream of the rotor to the rotor plane, and its implementation is as follows. During the aeroelastic simulations, the wind turbine model is subjected to a time history of turbulent wind generated with a first random seed. Next, a different turbulent field is generated by using a second seed, and the LiDAR simulator is fed at each instant of time and at each point in space with time histories of the blended wind given by Eq. (5). This way the measurement provided by the LiDAR sensor is polluted by an additional source of coherent noise, that would not be present when assuming Taylor's frozen hypothesis. The impact of this more realistic wind measurement on the performance of the predictive controllers will be analyzed in the results section.

## 3. Predictive control laws

### *3.1. Reduced models*

A non-linear wind turbine reduced model that reasonably captures the lowest spectrum of the machine response can be formulated as:

$$(J_r + J_g)\dot{\Omega} + Q_l(\Omega) + Q_e - \frac{1}{2}\rho V^2 A R C_Q(\beta, \lambda, V_m) = 0, \tag{6a}$$

$$m_t \ddot{d} + c_t \dot{d} + k_t d - \frac{1}{2}\rho V^2 A C_T(\beta, \lambda, V_m) = 0, \tag{6b}$$

$$\ddot{\beta} + 2\xi\omega\dot{\beta} + \omega^2(\beta - \beta_c) = 0, \tag{6c}$$

$$\dot{Q}_e + \frac{1}{T_e}(Q_e - Q_{e_c}) = 0, \tag{6d}$$

$$\dot{\nu} - \Omega = 0, \tag{6e}$$

and written more synthetically in first order form as

$$\boldsymbol{f}(\dot{\boldsymbol{x}}, \boldsymbol{x}, \boldsymbol{u}) = 0. \tag{7}$$

Equation (6a) expresses the dynamic torque balance of the rotor, while Eq. (6c) the tower fore-aft dynamic equilibrium. Equation (6c) is a second order pitch actuator model, and Eq. (6d) a first order torque actuator model. Finally, Eq. (6e) is an integral equation for the rotor angular speed $\Omega$, where $\nu = \int_{t-\Delta t}^{t} \Omega \mathrm{d}t$ is an integral state, useful for reducing the steady state trim error in the presence of model mismatch.

The state and input vectors $\boldsymbol{x}$ and $\boldsymbol{u}$ in Eq. (7) are defined as

$$\boldsymbol{x} = (d, \dot{d}, \Omega, \nu, \beta, \dot{\beta}, Q_e)^T, \tag{8a}$$

$$\boldsymbol{u} = (\beta_c, Q_{e_c})^T, \tag{8b}$$

where the state array is composed by the fore-aft displacement of the tower top $d$ and its time derivative $\dot{d}$, the rotor speed $\Omega$ and its integral $\nu$, the collective pitch angle $\beta$ and its time derivative $\dot{\beta}$ and, finally, the electrical generator torque $Q_e$. The input vector $\boldsymbol{u}$ is made up of the commanded collective pitch $\beta_c$ and commanded electrical torque $Q_{e_c}$. In Eqs. (6a,6c), the aerodynamic torque coefficient is noted $C_Q$ while the thrust coefficient is $C_T$. Both coefficients are pre-computed by means of a BEM model and stored in table-look-up form in terms of the blade pitch $\beta$ and effective tip-speed-ratio $\lambda = \Omega R/(V - \dot{d})$, where $V$ is the effective turbulent wind speed; optionally, both can be further scheduled in terms of a moving average mean wind speed $V_m$, to account for the effects of varying rotor deformation across the operating envelope of the machine. The rotor-shaft assembly has a rotational inertia $J_r$, while the one of the generator reduced to the low speed shaft is $J_g$. The torque loss due to the effects of mechanical friction is modeled by the torque load term $Q_l$. Finally, $m_t$, $c_t$ and $k_t$ are the effective mass, damping and stiffness, respectively, of the fore-aft dynamic model of the tower top, based on a modal description of the tower dynamics truncated at the first mode.

Given a trim condition specified by the set $\{\boldsymbol{x}^*, \boldsymbol{u}^*, V_m^*\}$, where $\boldsymbol{x}^*$, $\boldsymbol{u}^*$ and $V_m^*$ are the state and control vectors as well as the wind speed at that set point, Eq. (7) can be linearized as:

$$\Delta\dot{\boldsymbol{x}} = \boldsymbol{A}(\boldsymbol{x}^*, \boldsymbol{u}^*, V_m^*)\Delta\boldsymbol{x} + \boldsymbol{B}(\boldsymbol{x}^*, \boldsymbol{u}^*, V_m^*)\Delta\boldsymbol{u} + \boldsymbol{G}(\boldsymbol{x}^*, \boldsymbol{u}^*, V_m^*)\Delta\boldsymbol{w}, \tag{9}$$

where $\Delta\boldsymbol{x} = \boldsymbol{x} - \boldsymbol{x}^*$ and $\Delta\boldsymbol{u} = \boldsymbol{u} - \boldsymbol{u}^*$, while $\Delta\boldsymbol{w} = \boldsymbol{w} - \boldsymbol{w}^*$ is an exogenous wind input disturbance and $\boldsymbol{w}$ are wind describing states. In this work, $\Delta\boldsymbol{w} = V - V_m^*$, and the sole wind speed is considered. In turbulent wind conditions, $V_m^*$ is a slowly varying moving average of the effective turbulent wind speed $V$, that captures the set point around which the machine is operating. In this sense, system (9) represents a parameter varying wind-scheduled linear model. It would be possible to consider a more comprehensive list of wind disturbances in $\Delta\boldsymbol{w}$, capable of better describing the incoming wind field by accounting, for example, for wind shears; while it is in principle possible by a LiDAR to estimates such quantities [22], this idea is not pursued further in the rest of this work.

Although the behavior of a wind turbine is non-linear if considered over the full range of possible operative wind speeds, the nonlinearity can be dealt with effectively by wind scheduling the coefficients of the system matrices obtained by linearization at a sufficient number of trim points. To illustrate this point, Fig. 3 shows the coherence (computed as previously described) of some of the states as obtained from the closed loop integration in turbulent wind of the non-linear model (7) and of the linearized wind-scheduled model (9). In

these trials both models were regulated by the same feedback controller. The tests covered widely different mean wind speeds, spanning the partial and full regions, as well as transitions between the two.

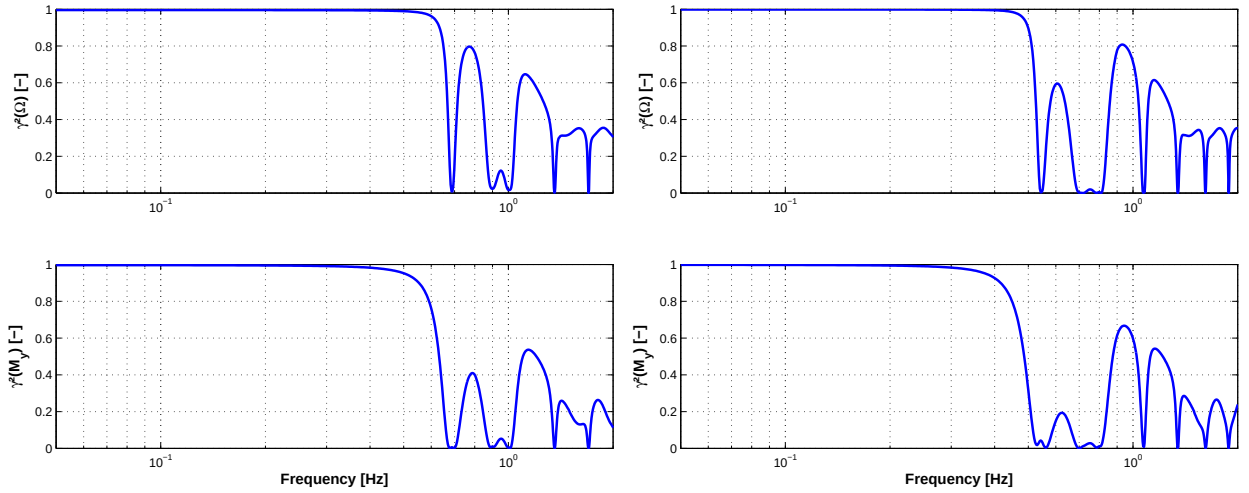


(a) (b)

Figure 3: Coherence diagrams for 600 sec simulations in IEC category A turbulent wind, for rotor speed $\Omega$ (top) and tower base fore-aft moment $M_y$ (bottom) obtained using non-linear and linearized wind-scheduled models. (a) Average wind speed of 11 m/sec. (b) Average wind speed of 23 m/sec.

The good coherence at the lower frequencies shows that a proper wind scheduling of the linearized model allows one to capture at least the lower spectrum of the wind turbine response to a level of fidelity that seems appropriate for the purpose of synthesizing control laws. In fact, for both the fore-aft moment and the rotational speed, the two models are in good accordance up to a frequency of 0.5 Hz, which is larger than the first fore-aft and rotor revolution frequencies. This justifies the use of the previously described linearized model in the formulations that are presented next.

### *3.2. Receding horizon control*

The basic idea behind the RHC formulation is that of repeatedly solving a cost minimization problem over a finite prediction window of span $T_f$, that is shifted forward as time progresses. At the generic time instant $t$, the quadratic cost function is defined as

$$J = \frac{1}{2}\int_t^{t+T_f} (\Delta \boldsymbol{x}^T \boldsymbol{Q} \Delta \boldsymbol{x} + \Delta \boldsymbol{u}^T \boldsymbol{R} \Delta \boldsymbol{u})\, \mathrm{d}t + \frac{1}{2}\Delta \boldsymbol{x}^T (t+T_f) \boldsymbol{Q}_f \Delta \boldsymbol{x}(t+T_f), \tag{10}$$

and its minimization is subject to the linear parameter varying system dynamics (9). The wind disturbance $\Delta w = V - V_m^*$ is computed from the available LiDAR measurements as follows: the LiDAR wind estimate $V$ is available over the prediction window span $T_f$ as a sequence of steps of time length $T_c$, while $V_m^*$ is computed by a moving average of the past LiDAR wind estimates over a backward looking window of 30 sec. The linear

model matrices are pre-computed at trim points covering the entire operating envelope of the machine, and then interpolated at run time based on $V_m^*$. This constrained formulation can be augmented with additional inequality conditions, in the form $\boldsymbol{D}\Delta\boldsymbol{x} + \boldsymbol{E}\Delta\boldsymbol{u} \leq \boldsymbol{0}$, which may be helpful to account for desired features in the solution. In this work, inequality constraints were used to impose pitch rate limitations and maximum excursions.

Although there is no closed form solution to this optimization problem, it can be solved efficiently by transcribing the linearized dynamics over a temporal grid of the prediction window, using a time marching scheme. By expressing the cost and constraints in terms of the resulting discrete values of inputs and states over the computational grid, one obtains an algebraic quadratic problem, which can be solved efficiently with ad hoc algorithms. In this work, the process of transcription and solution was performed with the code `CVXGEN` [16].

In order to limit the size, and hence the cost, of the optimization problem, one should limit the number of time steps covering the prediction window span $T_f$. A number of 10 steps was selected in the present analysis since, in combination with the present number of states and inputs, it leads to a problem size that is manageable by `CVXGEN` and to a cost that is well below real-time requirements (see later on for details). The number of time steps in turn limits the length of the prediction window, as the length of each time step cannot be too high for reasons of numerical accuracy and stability in the time integration of the system dynamics. However, it was found that the use of long prediction windows is typically not useful, so that this limitation does not hamper the performance of the RHC algorithm [27]. In fact, a parametric study was conducted on the virtual model of a 3.0 MW machine to find the best length $T_f$ of the prediction window. The analysis considered peak-to-peak differences of the fore-aft bending moment at the tower base and of the rotor speed for IEC gusty conditions [28], as well as power standard deviation and tower base fatigue in IEC category A turbulent wind conditions [29]. The best results were obtained for a rather short prediction window $T_f = 1$ sec. It should be pointed out that, with a varying mean wind speed, a fixed overall length of the prediction window implies a varying preview length in front of the rotor; again this was not found to play an important role, and so the adjustment of the prediction window with the wind speed was not considered to be necessary.

### *3.3. Non-homogeneous LQR control*

Using here again the linearized model (9) and cost function (10), under the hypothesis of an infinite prediction window span, $T_f \to \infty$, and of a stabilizable controlled system, in the absence of further inequality constraints, the minimum cost problem can be solved in closed form (see Ref. [15] and references therein for details), giving

$$\Delta\boldsymbol{u}(t) = -\boldsymbol{R}^{-1}\boldsymbol{B}^T\boldsymbol{P}\Delta\boldsymbol{x}(t) - \boldsymbol{R}^{-1}\boldsymbol{B}^T\int_t^\infty e^{-\bar{\boldsymbol{A}}^T(t-\tau)}\boldsymbol{P}\boldsymbol{G}\Delta\boldsymbol{w}(\tau)\,\mathrm{d}\tau. \tag{11}$$

Matrix $\boldsymbol{P}$ represents the solution of the steady state algebraic Riccati equation, so that the first term of the control input is the same of a classical LQR formulation. On the other hand, the second term, where $\bar{\boldsymbol{A}} = \boldsymbol{A} - \boldsymbol{B}\boldsymbol{R}^{-1}\boldsymbol{B}^T\boldsymbol{P}$, depends upon the wind disturbance $\Delta\boldsymbol{w}(\tau)$ over the infinite prediction window, and hence it represents the predictive part of the control law.

Although, in contrast to the RHC case, it is not possible to include actuation constraints in the formulation, the controller feels the characteristic times of the pitch and torque actuators through the reduced model, by Eqs. (6c,6d). In all simulation presented later on, the computed control inputs were fed to a high-fidelity aeroservoelastic model of the machine, so that even in the absence of rate or limit input constraints in the controller, actuation is performed by the machine virtual model accounting for all such limits.

In this work, the wind disturbance is assumed to be constant, i.e. $\Delta\boldsymbol{w}(\tau) = \Delta\boldsymbol{w}\ \forall\tau \in [t, \infty]$, so as to simplify the computation of the predictive term. Under this hypothesis, the integral in the second term of the control input expression can be computed in closed form, yielding

$$\boldsymbol{\Delta u}_{NH} = -\boldsymbol{R}^{-1}\boldsymbol{B}^T\bar{\boldsymbol{A}}^{-T}\boldsymbol{P}\boldsymbol{G}\boldsymbol{\Delta w}, \tag{12}$$

where $\boldsymbol{\Delta u}_{NH}$ is the non-homogeneous component of the control action. Therefore, the gain of the predictive control component can be pre-calculated at given trim points and then interpolated at run-time in terms of the mean wind speed $V_m^*$; the same is clearly true also for the LQR component of the control action.

From the available LiDAR measurements, the computation of the step wind input $\Delta w = V - V_m^*$ that feeds the predictive component of NHLQR, is performed as follows. The current effective wind speed $V$ is estimated at every call to the controller by averaging over a forward looking window of length $T_f$ the LiDAR wind estimate $V(\tau)$, that is made up by a sequence of steps of time length $T_c$. On the other hand, $V_m^*$ is computed by a moving average of the past LiDAR wind estimates, over a backward looking window of 30 sec.

In order to tune the length of the prediction window $T_f$ of the NHLQR controller, a parametric study was performed [28] in various deterministic and non-deterministic wind conditions, similarly to the RHC case. Here again the best compromise was determined to be $T_f = 1$ sec. This result may be not of general applicability, and might be specific to the characteristics of the LiDAR and wind turbine considered here. On the other hand, the relatively short size of the controller prediction window $T_f$ highlights the fact that, at least for the case considered here, it is not important to know what the wind will be many seconds in the future, but only its short term future evolution. Given the continuous update of the control solution and the presence of an elevated disturbance level, this result makes physical sense and it is in accordance with intuition.

## 4. Results

In order to verify the performance of the controllers and the effect of their free parameters, simulations in IEC gusty and turbulent wind fields [29] were carried out using the finite element multibody aeroservoelastic simulation code `Cp-Lambda` [30]. Two different machines were used in this study: a typical contemporary 3.0 MW wind turbine and a much larger 10.0 MW one, which is representative of possible future designs. The aerodynamic torque $C_Q$ and thrust $C_T$ coefficients appearing in the reduced model (7) were computed by using the `Cp-Lambda` code, and tabulated as functions of the blade pitch $\beta$ and tip-speed-ratio.

Three different controllers were considered: a standard LQR (i.e., the NHLQR controller without the predictive term), which was used to provide a reference non-predictive control solution, and the predictive RHC and NHLQR. All controllers operated at a control frequency of 50 Hz on both machines.

Weight matrices and references of the LQR-type controllers were computed at 12 trim wind speeds from 3 to 25 m/sec, and interpolated as functions of a 30 sec moving averaged wind signal; for the LQR controller, this signal is provided by the onboard anemometer, while for NHLQR the signal is obtained from a moving average of the LiDAR measurements. The selection of the control design parameters was based on trial and error process, by looking at the standard deviation of the rotor speed and power, as well as fatigue at tower base in category A turbulent wind conditions, with average wind speeds ranging from 3 up to 25 m/sec. To simplify the control tuning procedure, the weights associated with the tower fore-aft displacement and the actuator states were set to zero.

Weight matrices of the RHC formulation were similarly wind-scheduled. A slowly varying wind speed $V_m^*$ was obtained from a 10 sec moving average of the past and present LiDAR measurements. Based on this quantity, matrices were readily obtained at run time from interpolation of the stored values. The same quantity was used to compute the wind disturbance $\Delta w = V - V_m^*$ at each point over the prediction window.

### *4.1. Deterministic gusts*

IEC one-year extreme operative gust (EOG-1yr) wind conditions were considered, ranging from 5 to 23 m/sec, every 2 m/sec. The prediction span for both NHLQR and RHC was $T_f = 1$ sec, while the LiDAR-provided wind information was updated every $T_c = 0.2$ sec, i.e. at a frequency of 5 Hz.

Figures 4 and 5 show the normalized peak-to-peak response of both the rotational speed (at left) and the tower base fore-aft bending moment (at right), across all considered reference speeds. Figure 4 reports the results for the 3.0 MW turbine, while Fig. 5 for the 10.0 MW one. All results are normalized with respect to values obtained in a constant wind condition at the same speed. Due to the "Mexican hat" shape of the gust, the rotor speed response features a maximum and a minimum respectively much above and below the corresponding trim value. As a consequence, the normalized peak-to-peak difference results in rather high

values; nonetheless, the maximum observed overspeed in all test conditions never exceeded 15% of the rated angular speed.

Both NHLQR and RHC clearly outperform the non-predictive LQR controller. On both turbines, the peak-to-peak rotational speed difference is effectively reduced by both predictive controllers in full power, RHC performing better than NHLQR. In the partial load region, improvements with respect to the non-predictive LQR controller are less interesting, especially for NHLQR. This is due to the limitations imposed to the pitch motion at lower wind speeds and to the tuning of the weight matrices, which in the case of RHC resulted in a more effective use of the torque input. Both predictive controllers show a significant improvement with respect to the non-predictive LQR on the fore-aft moment. Here again the performance of NHLQR is not as good as RHC in full power conditions, but still largely outperforms the baseline LQR.

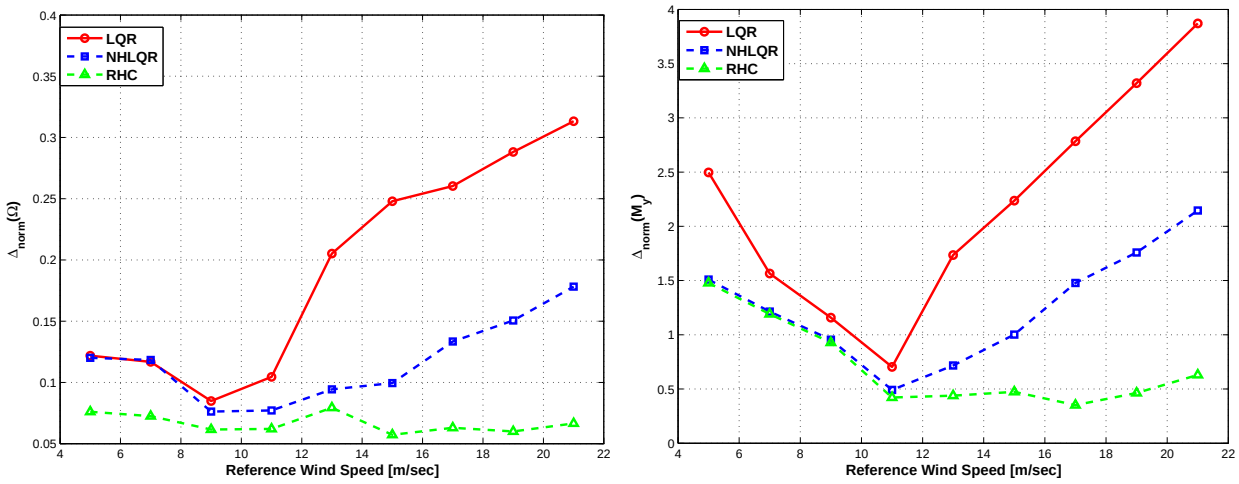


(a) (b)

Figure 4: Normalized peak-to-peak excursion of rotational speed (a) and tower base fore-aft bending moment (b), for simulations in IEC EOG-1yr wind conditions on the 3.0 MW machine.

### *4.2. Turbulent wind conditions*

The controllers were tested in IEC category A turbulent wind conditions of 600 sec of duration, with wind speeds ranging from 5 to 25 m/sec, covering the partial, transition and full power regions of both machines. To improve the statistical validity of the results, for every considered average wind speed, four turbulent wind time histories obtained with four different seeds were considered, and the results were then averaged. Furthermore, in order to prepare the unfrozen wind time histories, the same four wind histories were blended with four additional different histories as described previously. For the LiDAR simulator operating in unfrozen wind conditions, this resulted in a total of sixteen simulations for each considered average wind speed for the

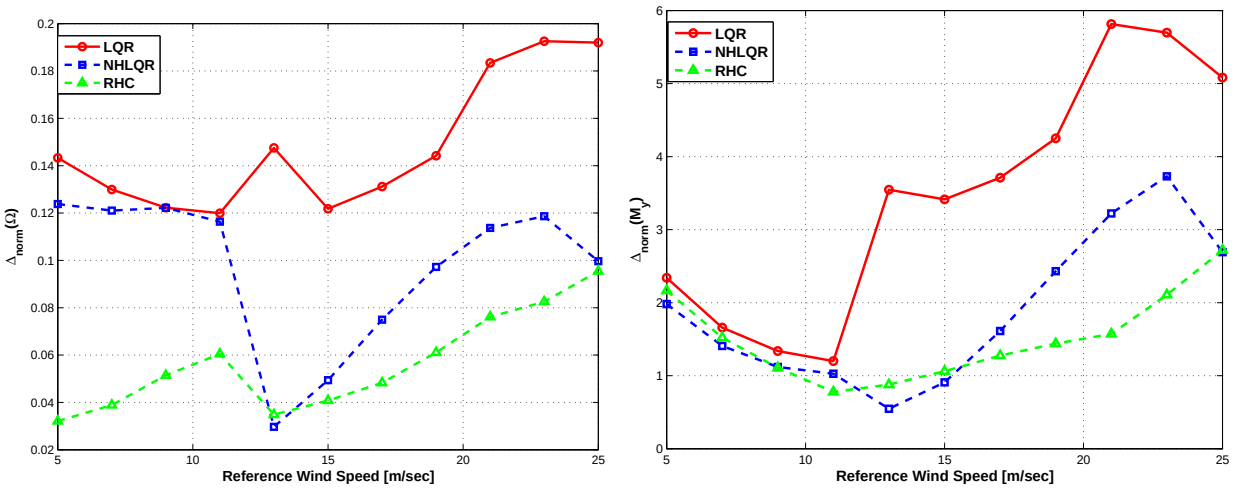


(a) (b)

Figure 5: Normalized peak-to-peak excursion of rotational speed (a) and tower base fore-aft bending moment (b), for simulations in IEC EOG-1yr wind conditions on the 10.0 MW machine.

two predictive controllers. The prediction window and the update time of the LiDAR sensor were set to the same values previously used for testing in deterministic conditions.

Figures 6 and 7 show the performance of the reference non-predictive LQR and of the two predictive controllers. The top row presents results for the standard deviation of power, which is a measure of the quality of the power output, while the bottom row shows tower base fatigue, measured by damage equivalent load (DEL). In the left column of the figures, power output is normalized with respect to the non-turbulent power at each considered wind speed, while tower base fore-aft DEL by a corresponding reference value. In order to better assess differences especially at the higher wind speeds, the plots in the right column of Figs. 6 and 7 present the same results normalized with respect to the performance of the LQR controller at each wind speed.

It can be observed that the standard deviation of power, which is larger in the partial load region where torque is used much more than collective pitch to control the turbine, is quite similar for the baseline LQR and NHLQR. The RHC controller provides some advantage for the low and high wind speeds, but slightly underperforms in the transition region, while NHLQR performs similarly to RHC in the full power region.

Furthermore, it can be noticed that the effects of this specific unfrozen turbulence model is generally almost negligible as also reported by other authors [22]. It remains to be seen whether the same conclusion would still hold true in conditions with non-uniform convection speeds, neglected in the present model, as it might be the case for high wind shears.

The results for the fore-aft moment are encouraging, especially at the higher wind speeds, where a visible

difference between the behavior of the predictive controllers and of the reference LQR can be noticed. NHLQR performs not as well as RHC, but nonetheless it is capable of effectively improving this figure of merit. For lower wind speeds the performance of both predictive controllers is similar, and the improvement with respect to the non-predictive algorithm is more modest. Here again, unfreezing the turbulence has limited effects.

For both turbines, a similar behavior of all controllers in different operational regions can be clearly noticed. In fact, notwithstanding any setting of the control weights, the control authority in the lower speed region is more modest, due to a limited pitch activity, and hence all controllers perform increasingly better on both power and loads as wind speed is increased.

From the plots at right in both Figs. 6 and 7, the predictive controllers appear quite capable in reducing both the power standard deviation and the tower base DEL on both turbines with respect to the baseline controller, more pronounced effects being visible for the larger and more flexible 10.0 MW turbine. Once more, the effect of unfreezing the turbulence model is not very relevant on the performance of the predictive controllers.

### *4.3. Computational cost*

In order to quantify the computational cost of the proposed formulations, the core routines of both controllers were isolated from the rest of the code, and each one was executed multiple times ($10^4$ and $10^8$ times, respectively, for RHC and NHLQR), so as to enhance the timing accuracy. Tests were run on a machine equipped with an `Intel`® `Core`™ `2 Duo E6550` 2.33 GHz processor with 2 GB RAM. The process was executed under `Windows Vista`™ `Business`, and monitored in order to ensure that there was no RAM saturation. Tests were executed 40 times, to avoid interference in the measurements due to potentially uncontrolled underlying processes, and the results were finally averaged to yield the execution time estimates.

The ratio between the execution time of RHC and NHLQR was found to be about 9730, with a rather low relative standard deviation of 3.6%. Although almost four orders of magnitude higher than NHLQR, the execution time of RHC was of about 6.4 milliseconds, i.e. well below the requirements for a 50 Hz activation frequency.

Further testing of the runtime performance involved a complete profiling of the core routines, in order to assess the computational cost of the two controllers in terms of floating point operations. Profiling was carried out using `Intel`® `VTune`™ `Amplifier XE 2013`. The resulting average ratio between the number of floating point operations of RHC and NHLQR was 10450, with a relative standard deviation of about 5.2%, based on 40 test runs. It is noteworthy that the RHC code generated by `CVXGEN` is more efficient by about a factor of 1.3 with respect to the NHLQR implementation, as can it be noticed by computing the ratio between floating point operations and execution time. Being tailored to the specific size and characteristic of a given optimal control problem, the code generated by `CVXGEN` is highly optimized and it makes use of

explicit directives wherever possible. This comes at the rather minor inconvenience of having to regenerate and recompile the code for any change in the parameters, as for example when the number of grid points used over the prediction window is modified.

## 5. Conclusions

This work has considered the design and implementation of two predictive controllers, exploiting future knowledge of the incoming wind speed provided by a LiDAR sensor. Both controllers were designed under the condition of being real-time capable, in the sense of having a reasonable computational cost for the typical activation frequencies onboard a wind turbine, and of necessitating of a fixed deterministic number of operations.

In order to work with realistic measurements of the predicted incoming wind, a generic LiDAR simulator was implemented and incorporated within the overall aeroservoelastic virtual simulation environment. It was found that the LiDAR operates a beneficial low pass filtering action on the wind measurements of the fast small turbulent eddies in the flow, which can not be affected by the controllers due to the intrinsic limits of full span collective pitch and torque actuation. The implementation included a formulation to unfreeze the wind field and avoid Taylor's hypothesis, which might potentially overestimate performance.

The two predictive controllers considered herein share a similar theoretical setup, being model-based optimal controllers seeking the minimum of a quadratic cost, and one can be interpreted as an approximation of the other. Since both are based on a wind-scheduled linear reduced model of the machine, a study was conducted so as to verify that such a model is indeed capable of representing the low frequency response of the wind turbine to a reasonable accuracy.

The two controllers were tested in gusty and turbulent wind conditions, using high fidelity aeroservoelastic models of two turbines of different sizes. In deterministic gusts, as expected, RHC greatly outperforms the non-predictive controller since, by seeing the incoming gust, can anticipate the control action; quite to the contrary, the non-predictive controller has to wait for the gust to engulf the rotor before it can react. Even the simpler NHLQR captures the essence of the preview information, delivering a performance that, although not as good as that of RHC, is significantly better than the baseline non-predictive LQR. In turbulent wind conditions, the benefits of LiDAR-enabled control are still noticeable, although to a reduced extent than in the deterministic case and only past the lowest wind speed region. This is also probably due in part to the inherent physical limits of collective full span pitch and torque actuation. Nonetheless, here again RHC improves on LQR while NHLQR places itself halfway between the two. In all cases, within the limits of the assumed turbulence evolution model, frozen or unfrozen wind fields appeared to imply modest changes in the results.

Finally, a measurement of the computational effort of the controllers showed a difference of about four orders of magnitude in favor of the simpler of the two, although the more sophisticated one was still much faster than required by a real-time implementation on rather standard computing hardware.

It is noteworthy, and initially apparently disappointing, that the increased complexity and computational cost of RHC is not balanced by a similar increase in performance. Besides the approximations which are evident in the formulation of NHLQR, the two predictive controllers differ mainly in the way they treat the predicted wind: RHC makes use of a detailed description of the wind disturbance over the prediction window, whereas NHLQR computes the predictive control component based on a rough constant average of the predicted wind. Furthermore, both controllers provide their best performance with relatively short prediction windows.

These facts suggest that, for this particular control problem, even rough approximations of the control problem are capable of capturing the essence of the preview information provided by the LiDAR sensor. For similar reasons, whatever the choice of the control algorithm, knowledge of the wind many seconds ahead of the rotor does not seem to be essential in order to get good control performance.

**Acknowledgements**

The present research was in part funded by the EU FP7 project INNWIND, whose support is gratefully acknowledged.

**References**

[1] P. Lindelöw, Fiber-based coherent LiDARs for remote wind sensing, Ph.D. thesis, Technical University of Denmark, 2008.

[2] A. Rettenmeier, O. Bischoff, M. Hofsäß, D. Schlipf, J.J. Trujillo, and M. Kühn, Wind field analyses using a nacelle-based LiDAR system, in: Proceedings of the European Wind Energy Conference (EWEC 2010), Warsaw, Poland, 2010.

[3] M. Sjöholm, T. Mikkelsen, L. Kristensen, J. Mann, P. Kirkegaard, S. Kapp, D. Schlipf, and J.J. Trujillo, Spectral analysis of wind turbulence measured by a doppler LiDAR for velocity fine structure and coherence studies, in: Proceedings of the International Symposium on Advancement of Boundary Layer Remote Sensing (ISARS), Saint Quentin-en-Yvelines, France, 2010.

[4] J. Laks, F. Dunne, and L. Pao, Feasibility studies on disturbance feedforward techniques to improve load mitigation performance, Technical Report NREL/SR-5000-48598, National Renewable Energy Laboratory (NREL), 2010.

[5] M. Soltani, R. Wisniewski, P. Brath, and S. Boyd, Load reduction of wind turbines using receding horizon control, Technical report, Department of Electronics Systems, Aalborg University, Aalborg, Denmark and Vestas Technology R&D, Aarhus, Denmark and Department of Electrical Engineering, Stanford University, Palo Alto, CA, USA, 2010.

[6] F. Dunne, L. Pao, A. Wright, B. Jonkman, and N. Kelley, Adding feedforward blade pitch control to standard feedback controllers for load mitigation in wind turbines, Mechatronics 21(2011) 682–690.

[7] E. Bossanyi, B. Savini, M. Iribas, M. Hau, B. Fischer, D. Schlipf, T. van Engelen, M. Rossetti and C.E. Carcangiu, Advanced controller research for multi-MW wind turbines in the UPWIND project, Wind Energy 15(2012) 119–145.

[8] D. Schlipf, D.J. Schlipf and M. Kühn, Nonlinear model predictive control of wind turbines using LIDAR, Wind Energy DOI:10.1002/we.1533 (2012).

[9] A. Koerber and R. King, Combined feedbackfeedforward control of wind turbines using state-constrained model predictive control, IEEE Transactions on Control Systems Technology 21(2013) 1117–1128.

[10] N. Wang, K.E. Johnson and A.D. Wright, Comparison of strategies for enhancing energy capture and reducing loads using LiDAR and feedforward control, IEEE Transactions on Control Systems Technology 21(2013) 1129–1142.

[11] A.A. Ozdemir, P. Seiler and G.J. Balas, Design tradeoffs of wind turbine preview control, IEEE Transactions on Control Systems Technology 21(2013) 1143–1154.

[12] M. Kristalny, D. Madjidian and T. Knudsen, On using wind speed preview to reduce wind turbine tower oscillations, IEEE Transactions on Control Systems Technology 21(2013) 1191–1198.

[13] K.A. Kragh, M.H. Hansen and T. Mikkelsen, Precision and shortcomings of yaw error estimation using spinner-based light detection and ranging, Wind Energy DOI:10.1002/we.1492 (2012).

[14] C.L. Bottasso, A. Croce, B. Savini, W. Sirchi, and L. Trainelli, Aero-servo-elastic modeling and control of wind turbines using finite element multibody procedures, in: Proceedings of the ECCOMAS Multibody Dynamics 2005 Thematic Conference, Madrid, Spain, June 21–24, vol. 16, pages 291–308, 2006.

[15] R.D. Hampton, C.R. Knospe, and M.A. Townsend, A practical solution to the deterministic nonhomogenous LQR problem, Journal of Dynamic Systems, Measurements and Control 118(1996) 354–359.

[16] J. Mattingley and B. Stephen, CVXGEN: A code generator for embedded convex optimization, Technical report, Electrical Engineering Department, Stanford University, Palo Alto, CA, 2010.

[17] J. Schuurmans, E. Nederkoorn, S. Kanev, R. Rutteman, and E. Nguyen, Optimised aerodynamics and control by nonlinear model based predictive control, in: Proceedings of EWEA 2013, Vienna, Austria, 2013.

[18] D. Schlipf, D. Trabucchi, O. Bischoff, M. Hofsäß, J. Mann, T. Mikkelsen, A. Rettenmeier, J.J. Trujillo, and M. Kühn, Testing of frozen turbulence hypothesis for wind turbine applications with a scanning LiDAR system, in: Proceedings of the International Symposium on Advancement of Boundary Layer Remote Sensing (ISARS), Saint Quentin-en-Yvelines, France, 2010.

[19] E. Simley, L. Pao, R. Frehlich, B. Jonkman, and N. Kelley, Analysis of wind speed measurements using continuous wave LiDAR for wind turbine control, in: Porceedings of the 49th AIAA Aerospace Sciences Meeting including the New Horizons Forum and Aerospace Exposition, Orlando, FL, USA, 4–7 January, 2011.

[20] G.I. Taylor, The spectrum of turbulence, Proceedings of the Royal Society A 164(1938) 476–490.

[21] E. Bossanyi, Un-freezing the turbulence: improved wind field modelling for investigating LiDAR-assisted wind turbine control, in: Proceedings of the European Wind Energy Conference (EWEC 2012), Bruxelles, Belgium, 2012.

[22] E. Bossanyi, A. Kumar, and O. Hogues-Salas, Wind-turbine control application of turbine mounted LiDAR, in: Proceedings of Torque 2012 — The Science of Making Torque from Wind, Oldenburg, Germany, 2012.

[23] L.R. Rabiner, and B. Gold, Theory and Application of Digital Signal Processing, Prentice-Hall, Englewood Cliffs, NJ, 1975.

[24] P.D. Welch, The use of fast Fourier transform for the estimation of power spectra: a method based on time averaging over short, modified periodograms, in: IEEE Transactions on Audio and Electroacoustics 15(1967) 70–73.

[25] L. Kristensen, On longitudinal spectral coherence, Boundary Layer-Meteorology 16(1979) 145–153.

[26] P. Veers, Three dimensional wind simulation, Technical report SAND88-0152, Sandia National Laboratories, 1988.

[27] Y. Wang and S. Boyd, Fast model predictive control using online optimization, IEEE Transactions on Control Systems Technology 18(2010) 267–278.

[28] G. Giansiracusa, Tecniche di controllo predittivo per aerogeneratori con ausilio di strumentazione LiDAR, M.Sc. thesis (in Italian), Dipartimento di Ingegneria Aerospaziale, Politecnico di Milano, Milano, Italy, 2011.

[29] Wind Turbines — Part 1: Design Requirements, Ed. 3.0, International Standard IEC 61400-1, 2005.

[30] C.L. Bottasso and A. Croce, Cp-Lambda: User's manual, Technical report, Dipartimento di Ingegneria Aerospaziale, Politecnico di Milano, 2006–2014.

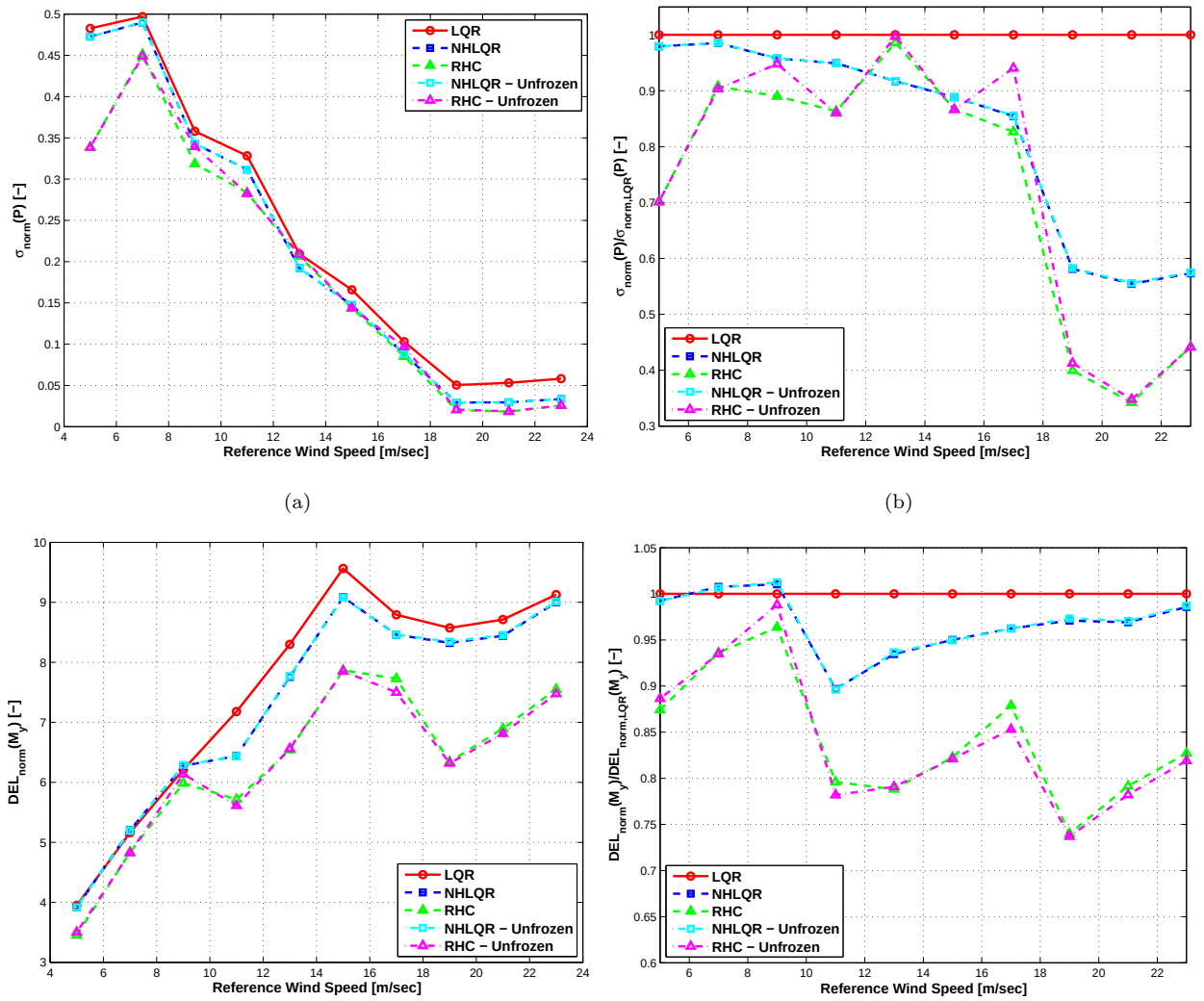


(a) (b)

(c) (d)

Figure 6: Power standard deviation (top row) and tower-base fore-aft DEL (bottom row), for the 3.0 MW turbine in IEC category A turbulent wind conditions. The same performance indices are normalized with respect to the LQR results on the right column of the figure.

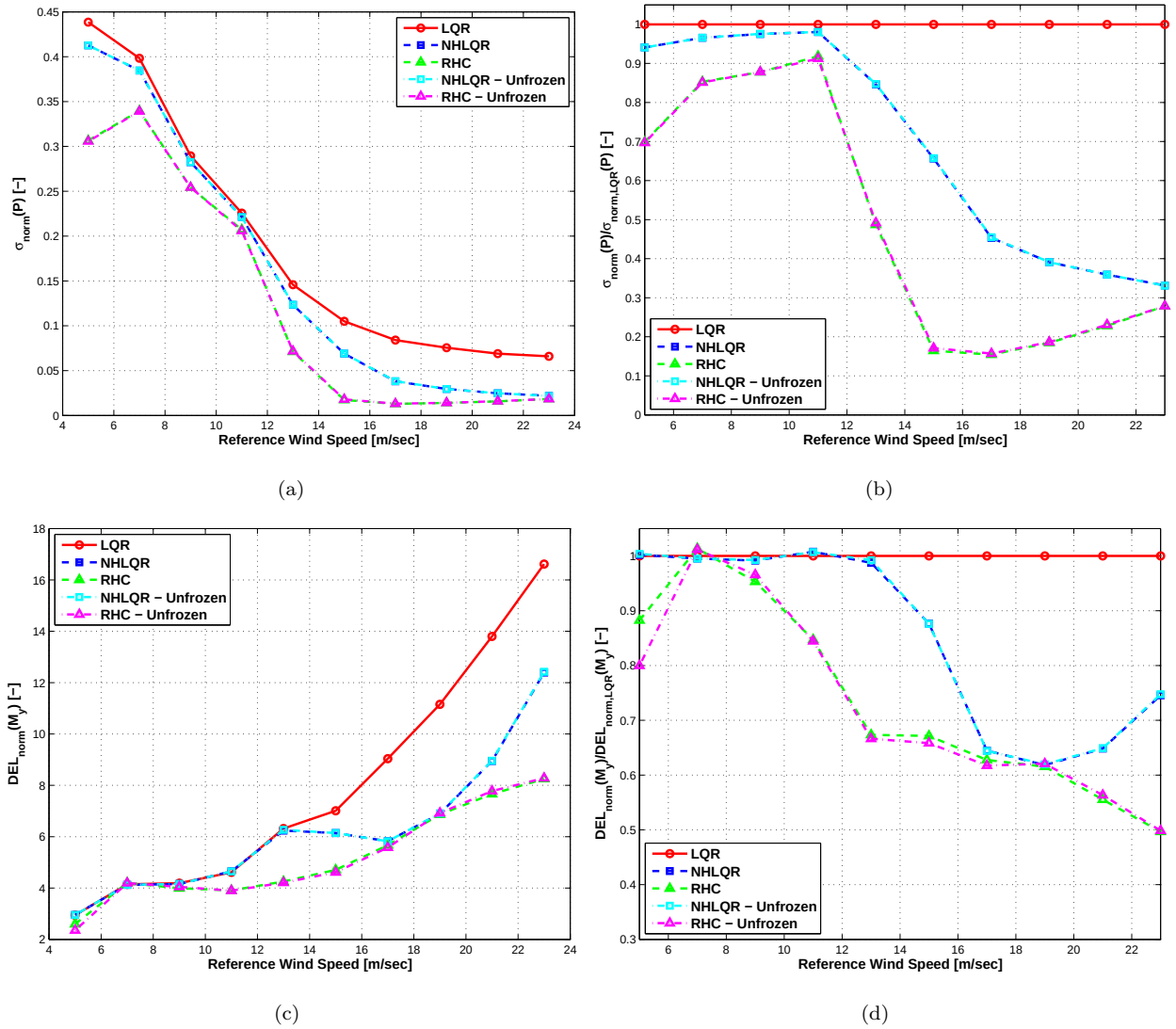


Figure 7: Power standard deviation (top row) and tower-base fore-aft DEL (bottom row), for the 10.0 MW turbine in IEC category A turbulent wind conditions. The same performance indices are normalized with respect to the LQR results on the right column of the figure.